Nitrogen-Vacancy Magnetic Relaxometry of Nanoclustered Cytochrome C Proteins

Journal:	*Nano Letters*
Manuscript ID	nl-2023-03843y.R3
Manuscript Type:	Communication
Date Submitted by the Author:	n/a
Complete List of Authors:	Lamichhane, Suvechhya; University of Nebraska-Lincoln, Department of Physics and Astronomy and the Nebraska Center for Materials and Nanoscience Timalsina, Rupak; University of Nebraska-Lincoln, Mechanical & Materials Engineering Schultz, Cody; University of Nebraska-Lincoln, Department of Chemistry Fescenko, Ilja; University of Latvia Ambal, Kapildeb; Wichita State University, Physics Liou, Sy-Hwang; University of Nebraska-Lincoln, Department of Physics and Astronomy and the Nebraska Center for Materials and Nanoscience Lai, Rebecca; University of Nebraska-Lincoln, Chemistry Laraoui, Abdelghani; University of Nebraska-Lincoln, Mechanical & Materials Engineering; University of Nebraska-Lincoln, Department of Physics and Astronomy and the Nebraska Center for Materials and Nanoscience

Nitrogen-Vacancy Magnetic Relaxometry of Nanoclustered Cytochrome C Proteins

Suvechhya Lamichhane,[1] Rupak Timalsina,[2] Cody Schultz,[3] Ilja Fescenko,[4] Kapildeb Ambal,[5] Sy-Hwang Liou,[1] Rebecca Y. Lai,[3] and Abdelghani Laraoui[1,2,*]

[1]*Department of Physics and Astronomy and the Nebraska Center for Materials and Nanoscience, University of Nebraska-Lincoln, Lincoln, Nebraska 68588, USA*
[2]*Department of Mechanical & Materials Engineering, University of Nebraska-Lincoln, Lincoln, NE 68588, USA*
[3]*Department of Chemistry, University of Nebraska-Lincoln, Lincoln, NE 68588, USA*
[4]*Laser Center, University of Latvia, Riga, LV-1004, Latvia*
[5]*Department of Mathematics, Statistics, and Physics, Wichita State University, Wichita, KS 67260, USA*
[*]*Corresponding Author E-mail: alaraoui2@unl.edu*

ABSTRACT: Nitrogen-vacancy (NV) magnetometry offers an alternative tool to detect paramagnetic centers in cells with a favorable combination of magnetic sensitivity and spatial resolution. Here, we employ NV magnetic relaxometry to detect cytochrome C (Cyt C) nanoclusters. Cyt-C is a water-soluble protein that plays a vital role in the electron transport chain of mitochondria. Under ambient conditions, the heme group in Cyt-C remains in the Fe^{+3} state which is paramagnetic. We vary the concentration of Cyt-C from 6 μM to 54 μM and observe a reduction of the NV spin lattice relaxation time (T_1) from 1.2 ms to 150 μs, attributed to the spin noise originating from the Fe^{+3} spins. NV T_1 imaging of Cyt-C drop-casted on a nanostructured diamond chip allows us to detect the relaxation rates from the adsorbed Fe^{+3} within Cyt-C.

KEYWORDS: *Nitrogen-vacancy, relaxometry, cytochrome C, iron, paramagnetic*

Cytochromes, including cytochrome C (Cyt-C), are redox-active proteins involved in the electron transport chain (ETC) and redox catalysis.[1] It is a water-soluble protein with a molecular weight of 13 kDa typically located in the inter-mitochondrial membrane.[1,2] The main function of Cyt-C within the mitochondria is to serve as an intermediate electron receptor during respiration, facilitating the transfer of electrons between Complex III and Complex IV in the ETC.[1] The electron transfer involves the reduction of the oxidized Cyt-C (Fe^{+3}) heme group to Fe^{+2} by an electron from Complex III. Subsequently, Cyt-C releases the electron to Complex IV, and the Fe center returns to the oxidized Fe^{+3} state.[3] During cell necrosis and apoptosis, Cyt-C is released from the mitochondria, which leads to the non-inflammatory activation of apoptotic protease activating factor 1, eventually cascading to caspase-9 activation and the execution-phase of the cell.[4] The concentration of Cyt-C decreases in the mitochondria and increases in the cytosol during apoptosis, resulting in variations of Cyt-C amounts depending on the specific cellular region being analyzed.[1,2]

While the intracellular release of Cyt-C is not associated with inflammation, its release into the extracellular matrix has been correlated with inflammatory conditions and cellular damage. Studies on rats resuscitated after ventricular fibrillation showed a tenfold increase in plasma Cyt-C, with the survival outcome inversely correlated to plasma Cyt-C concentrations.[5] Increased Cyt-C levels have also been linked to liver disease, liver damage, and kidney damage.[6,7] Therefore,

plasma Cyt-C can be a useful diagnostic tool for pathogen-associated or danger-associated molecular patterns.[2]

Numerous techniques have been utilized to detect Cyt-C, including electron paramagnetic resonance (EPR) spectrometry[8–10] and X-ray photoelectron spectroscopy (XPS).[11,12] The variation of the Cyt-C concentration in the cells depending on its current physiology state makes it hard to use bulk techniques such as EPR to detect it at the sub-cellular level. Among the currently available high-sensitivity and spatial resolution detection techniques, magnetic imaging based on the nitrogen-vacancy (NV) center in diamond[13–18] emerges as one of the most promising tools for high-resolution nanoscale imaging. The NV center is a spin-1 defect with optically addressable electron spin properties[19–21] and millisecond spin relaxation times (T_1, T_2) at room temperature.[22] These capabilities have opened new opportunities in quantum sensing,[23] nanoscale magnetometry,[24–26] and biosensing.[27] For example, it enabled the initial detection of single proteins[28] and the realization of nanoscale nuclear magnetic resonance (NMR) spectroscopy.[29–32] NV magnetometry has been used very recently to measure the magnetic properties of individual (size < 1 μm) malarial hemozoin biocrystals[18] and $[Fe(Htrz)_2(trz)](BF_4)$ spin crossover molecules.[13] Another approach of NV magnetometry is to detect spin noise from metal ions through the decrease of the spin-lattice T_1 relaxation time. NV T_1 relaxometry has been used to detect Gd^{+3} ions,[33] Cu^{+2} ions,[34] and more recently to map Fe^{+3} in ferritin proteins.[16,17] There have been several studies using NV relaxometry in the biomedical field to study free radicals present in single mitochondria,[35] endothelial cells,[36] dendritic cells,[37] and virus-infected cells,[38] providing great insights on understanding the cellular metabolism.

In this study, we employ NV T_1 relaxometry to detect the concentration variations in Cyt-C nanoclusters (diameter: 50 – 200 nm, height: 5 – 15 nm) through the paramagnetic Fe^{+3} centers. The changes in Cyt-C concentration directly impact T_1, facilitating a quantitative detection of Cyt-C levels. To achieve this, we systematically altered the amount of Cyt-C adsorbed on the diamond chip, ranging from 6 μM to 54 μM through drop-casting. The observed reduction in T_1 from ~ 1.2 ms to < 200 μs is attributed to the spin-noise generated by the Fe^{+3} centers present within Cyt-C. NV T_1 imaging of Cyt-C nanoclusters, drop-casted on a functionalized nanostructured diamond chip, allows us to deduce the relaxation rates caused by the adsorbed Fe^{+3} of a density in the range of 1.44×10^6 to 1.7×10^7 per μm^2 within Cyt-C.

The Fe^{+3} center in Cyt-C is coordinated to four nitrogen atoms,[1] forming the heme ring as depicted in Figure 1a. Additionally, Fe^{+3} coordinates with methionine and histidine, resulting in a hexacoordinated configuration.[3] Notably, the sulfur atom from methionine acts as a strong-field ligand, causing the heme complex to exhibit a low spin state (S = ½) under ambient conditions.[39] In this work, we use horse heart Cyt-C powder purchased from Sigma Aldrich (molecular weight = 12,384 g/mol). As received, Cyt-C powder is predominantly in the oxidized state Fe^{+3} and diluted in deionized (DI) water with a density of 200 mg/ml (~ 16.1 mM, pH = 5). Cyt-C in its native state remains neither unfolded or denatured within a pH range of 3 to 7.[40,41]

To measure the diameter and height of Cyt-C nanoclusters, we further diluted the Cyt-C solution to a concentration of ~ 0.1 mM and drop-casted 5 μL on silicon and diamond substrates, allowing it to evaporate and form a thin film. To alleviate the charging effects in SEM measurements,[42] we drop-casted Cyt-C nanoclusters on carbon tape[13] and on gold (Au) coated diamond substrates, see the Supporting Information (SI) Section S1. Figure 1b shows the SEM image of nanoclustered Cyt-C proteins on carbon tape with an aggregated diameter that varies from 30 nm to 150 nm (SI Section S1). The diameter of a single monomer of Cyt-C is reported to be ~ 3.4 nm.[43] However, due to surface interactions, when Cyt-C is drop-casted on the diamond

surfaces, it tends to agglomerate, resulting in larger nanoclusters. Remarkably, even at a lower concentration (≤ 2 μM), this agglomeration phenomenon is still observed on the diamond substrate with an average diameter of Cyt-C nanoclusters observed 100 ± 50 nm (Figure S1). Similar agglomeration effects have been reported across different concentrations of Cyt-C.[43] Despite its stability, even in its natural state Cyt-C tends to polymerize rather than remain in a monomeric state, possibly through aggregation.[44] AFM measurements of 2 μM Cyt-C solution drop-casted on top of the diamond substrate show a height of ~ 9 ± 6 nm (Figure 1c).

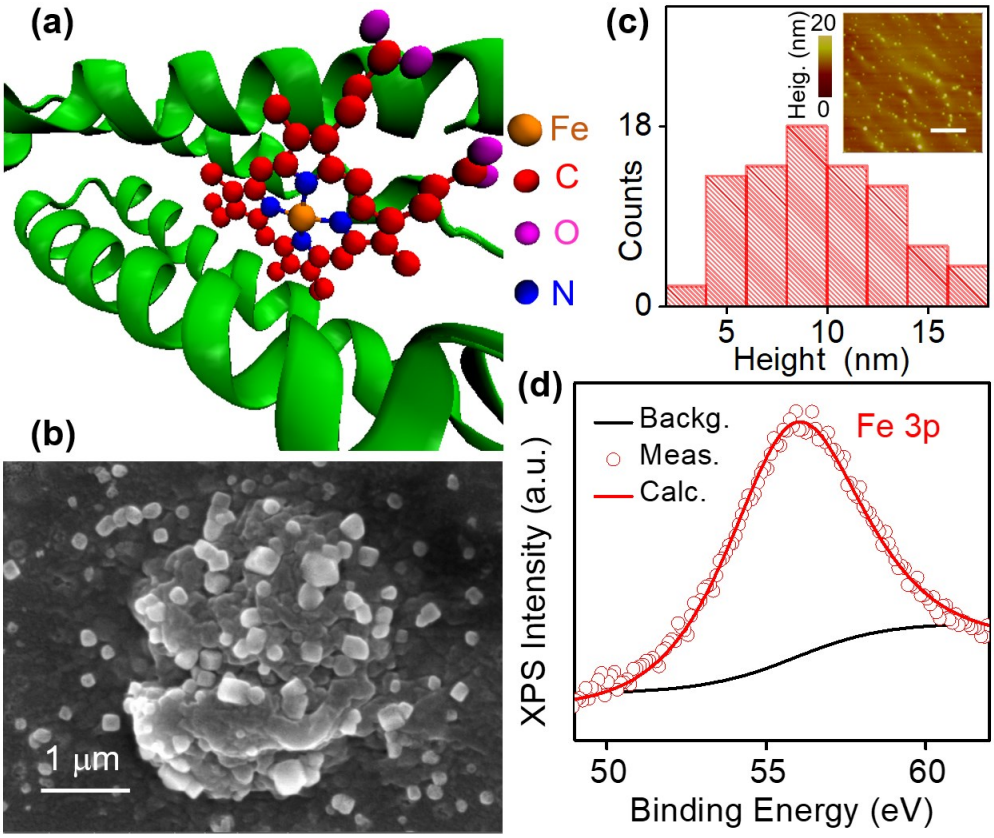

Figure 1. (a) Molecular structure of Cyt-C complex derived from reference [1]. (b) SEM image of 18 μM Cyt-C drop-casted on a carbon tape to prevent charging effect. (c) AFM height distribution of Cyt-C nanoclusters (concentration of 2 μM) drop-cased on top of the diamond substrate. The mean height of Cyt-C nanoclusters is ~ 9 ± 6 nm. Inset of (c): AFM image of the Cyt-C nanoclusters (the scale bar is 5 μm). (d) Measured (open circles) XPS spectra of Fe 3p in Cyt-C with the fitting (red solid line) showing the Fe^{+3} state. The background signal is plotted in the black solid line curve.

To further ensure the absence of impurities, XPS measurements were conducted (SI Section S2). We employed a high-resolution XPS by using a step size of 0.1 eV for the analysis of N, S, C, O, and Fe. Following the data acquisition, we conducted peak fitting using a combined Lorentzian and Gaussian function which allowed us to deconvolute the spectral feature and extract information regarding the chemical states and binding energy of the elements. Figure 1d shows the measured (open circles) and calculated (solid line) high-resolution spectra of Fe 3p. The spectra exhibit a distinct peak at a binding energy of 55.6 eV, indicative of the Fe oxidation state being +3.[45] Moreover, we corroborated the presence of Fe-sulfur bonds at binding energy of 167 eV through the examination of the high-resolution sulfur peak (Figure S2d).[46]

The negatively charged NV center in the diamond lattice is a substitutional nitrogen adjacent to a vacancy site (Figure 2b) with a spin triplet in the ground state that features a zero-field splitting D = 2.87 GHz between states m_s = 0 and m_s = ±1 (Figure 2c).[19,21] A green laser illumination (532 nm) yields spin-conserving excitation to the excited triplet state, which in turn leads to far-red photoluminescence (650 – 800 nm). Intersystem crossing to metastable singlet states takes place preferentially for NV centers in the m_s = ±1 states, ultimately resulting in an almost complete transfer of population to the m_s = 0 state.[19] Microwave (MW) excitation allows spin transitions from m_s = 0 to m_s = ±1 sublevels. The applied magnetic field breaks the degeneracy of the m_s = ±1, leading to a pair of spin transitions (m_s = 0 to m_s = +1 and m_s = 0 to m_s = -1) that can be interrogated *via* optically detected magnetic resonance (ODMR) spectroscopy.[13,18] This method results in a set of resonance peaks that are sensitive to magnetic field (Figure S5b). In addition, if the laser excitation is abruptly turned off, the amplitude of the ODMR signal decays exponentially as the NV electron spins relax from their polarized states. The rate of this decay (Γ_1) or relaxation time ($T_1 = 1/\Gamma_1$) depends on the weak random magnetic fields created by the diamond sensor itself and the external spin noise.[47,48] Measurements of the rate change in Γ_1 is the basis of NV-T_1 relaxometry which is used here to detect magnetic dipole-dipole interaction between NV spins and the fluctuating Fe^{+3} spins in Cyt-C nanoclusters.[49]

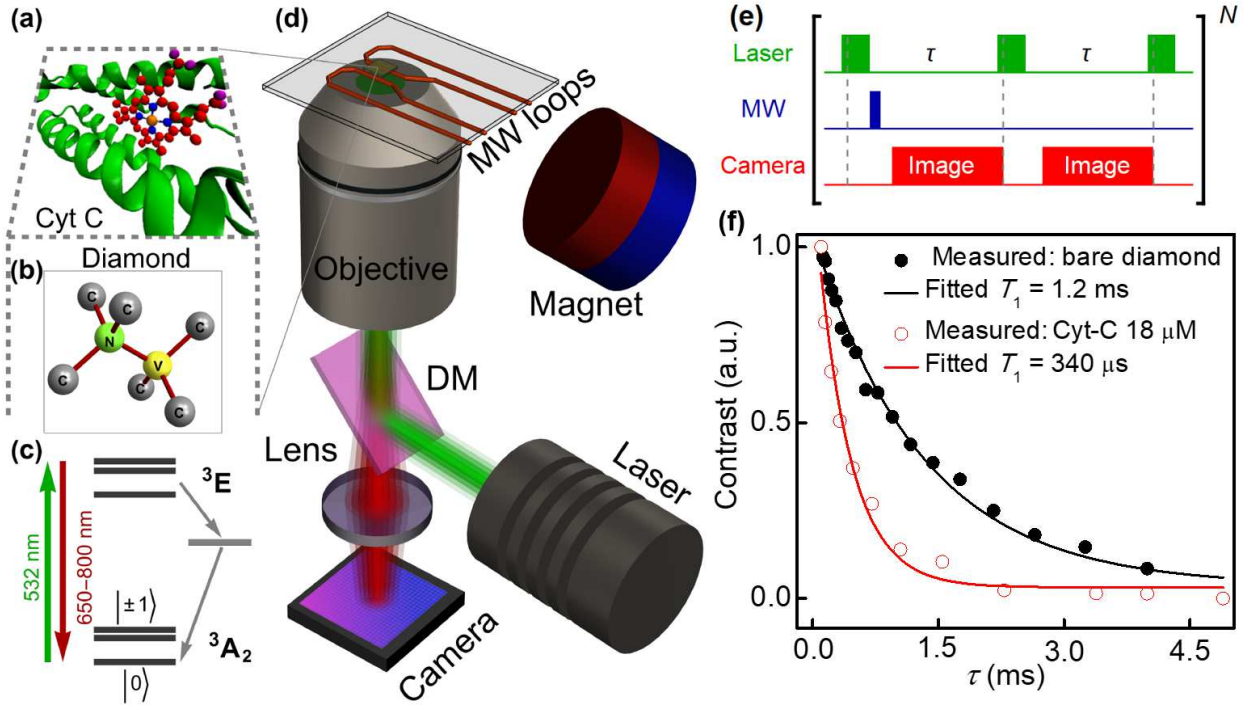

Figure 2. (a) Molecular structure of Cyt-C protein. (b) A schematic of the NV center inside the diamond lattice (nitrogen: green atom, yellow: vacancy). (c) A schematic of the energy levels of the NV center ground ($^3A^2$) and excited (^{3}E) states with intermediate metastable state. A green laser (532 nm) initializes the NV center spins and results in fluorescence in wavelength range of 650 – 800 nm. (d) A schematic of the widefield NV microscope used for T_1 relaxometry measurements and imaging of Cyt-C nanoclusters. DM is the dichroic mirror. (e) A schematic of a pulse sequence for T_1 relaxometry imaging. (f) T_1 curve measured on a bare diamond (filled circles) and after drop-casting 18 μM Cyt-C solution on diamond (open circles). The black and red solid lines are exponential decay function fits of the measured T_1 relaxation curves.

To make the NV sensor, we used 3 mm × 2.5 mm × 0.05 mm electronic grade (100) cut and polished diamond. A thin (~ 5 – 8 nm) NV sensing layer (Figure S5a) was created near the diamond surface by using $^{15}N^{+}$ implantation followed by high vacuum and high temperature annealing and then cleaning in a boiling tri-acid mixture (see SI Section S5 for more details).[18,31,50] To attach Cyt-C nanoclusters, we carboxylated the diamond surface with NV layer underneath (see SI Section S3). The adsorption of Cyt-C occurs through electrostatic attraction between the anionic groups ($-COO^{-}$) present in the carboxylated surface and the positively charged amino groups ($-NH^{3+}$), or through the formation of hydrogen bonds between $-NH^{3+}$ and CO^{-}.[51] Various concentrations of Cyt-C in DI water were drop-casted on the diamond substrate. We used DI water instead of other buffers to prevent any effects on T_1 from the salts and other compounds present in them.

In Figure 2d, we show the schematic of the widefield ODMR microscope. We used a 532 nm laser (power = 180 mW) to excite the NVs over an area of ~ 36 μm × 36 μm, and the NV fluorescence (650 – 800 nm) is mapped onto a sCMOS camera.[13,18] The diamond chip was placed on top of a glass coverslip with patterned gold loops for MW excitation (Figure 2d). A magnetic field B_{app} (3.2 mT) is applied along [111] direction of the (100) diamond enabling the separation of the ODMR peaks for m_s = 0 to m_s = -1 and m_s = 0 to m_s = +1 spin transitions (Figure S5b). Detailed information regarding the experimental setup is provided in SI Section S5.

The T_1-realxometry measurement protocol is depicted in Figure 2e and summarized here:[47,52] A laser pulse (5 μs) is used first to initialize the NV spins in the m_s = 0 state, then a MW π pulse is applied to flip the NV spins to $m_s = -1$ state, and finally, a readout laser pulse (5 μs) is applied after varying the measurement time τ. This sequence is followed by another sequence but without π pulse. The method and underlying physics are explained in references [47] and [52]. To optimize the timing, each readout laser pulse is used as an initialization pulse for the next sequence. The NV fluorescence is detected by a sCMOS camera, where exposure (4 ms) starts well before the laser pulse, so that the camera stops reading after the first microsecond of the laser induced fluorescence pulse. The first microsecond contains the ODMR contrast signal, which is maximal when the spins are just initialized into m_s = -1 or m_s = 0 states but decrease with increasing τ due to the relaxation of the NV spin polarization. We extract this contrast by pixelwise subtracting frames for NVs initialized into m_s = -1 (with π pulse) from NVs initialized into m_s = 0 state (without π pulse) then dividing them pixelwise by a sum of both frames. The pair of measurements is repeated $N = 10^4$ times for each value of the varying time τ (Figures S6b, S6c, and S6d). Figure 2f shows preliminary measurements of the ODMR contrast *vs* τ on bare diamond (filled circles) and after drop-casting 18 μM Cyt-C solution on diamond (open circles). The NV measurements are integrated over an area of 1296 μm^2, fitted with one exponential decay function to extract T_1 values (see SI Section S6). A reduction of T_1 from ~ 1.2 ms for the bare diamond to 340 μs after adding 18 μM Cyt-C is obtained and attributed to the spin-noise originating from Fe^{+3} spins present within the Cyt-C proteins.

To differentiate the effect of Fe^{+3} spins within the Cyt-C nanoclusters from other spin noises due to paramagnetic impurities[53,54] inside the diamond lattice and the diamond surface noise,[55] we performed T_1 relaxometry imaging on a nanostructured diamond chip with SiN grating (a separation distance of 4 μm and height of 50 nm). Such a grating is very robust against acids/chemicals during the repeated cleaning process in contrast to other polymers (*e.g.*, polymethyl methacrylate) which would degrade quickly.[34] See the SI Section S4 for the fabrication details. Regions covered with SiN act as barriers for direct dipolar interaction between NV centers and any spin noise on the diamond surface. We found that the SiN film reduces the Γ_1 rate of NV

spins underneath (Figures 3b and 3f) in comparison to conductive metal films (*e.g.* Al) where a strong Γ_1 increase was observed.[56]

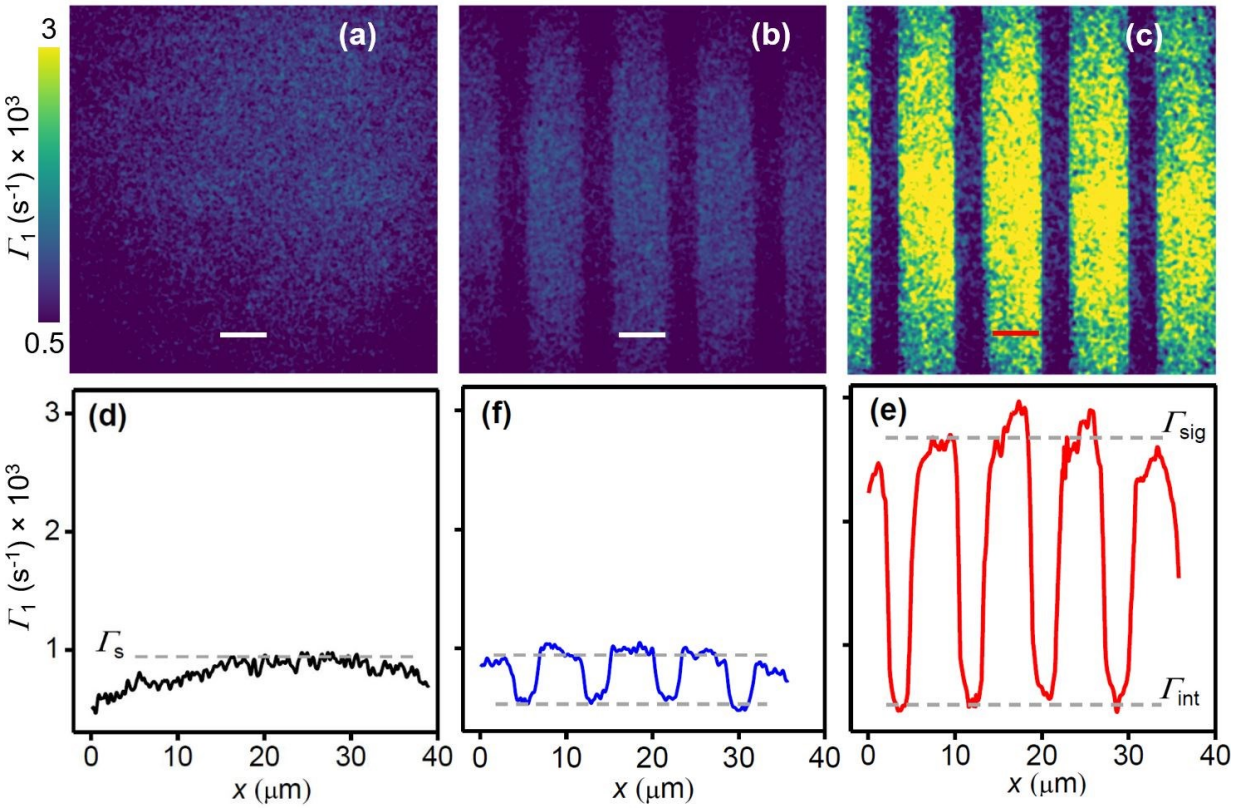

Figure 3. Γ_1 maps acquired by pixelwise exponential fitting of series of maps of the ODMR contrast decays for (a) clean bare diamond, (b) clean diamond with the SiN grating, and (c) Cyt-C with a concentration of 54 μM drop-casted on the diamond with SiN grating. The scale bar in (a), (b), and (c) is 5 μm. Corresponding extracted horizontal Γ_1 profiles from the measurements done on bare diamond (d), diamond with SiN grating and no Cyt-C (f), and diamond with SiN and Cyt-C (e), respectively.

Figures 3a, 3b, and 3c show Γ_1 images of the bare diamond, diamond with SiN grating (no Cyt-C), and diamond with SiN and Cyt-C, respectively. The Γ_1 images were obtained from a series of contrast decay images by pixel-by-pixel fitting with a single exponential function. For further analysis, we integrated Γ_1 images vertically to measure the Γ_1 profiles of the measured signals on bare diamond (Figure 3d), diamond with SiN grating and no Cyt-C (Figure 3f), and diamond with SiN and Cyt-C (Figure 3e). The maximum value of $\Gamma_1 = \Gamma_s$ (Figures 3d and 3f) obtained from uncovered clean areas of the NV sensors is $(0.91 \pm 0.05) \times 10^3$ s^{-1}. This value decreased towards the edges of the measurement spot due to a slight drop in the intensity of the laser beam, leading to a decrease in the ODMR contrast, which changed the estimation of Γ_1. To avoid this effect, we estimated the relaxation rates in the central part of the measurement fluorescence spot, where the laser intensity is relatively homogenous. The relaxation rate Γ_{int} is $(0.45 \pm 0.05) \times 10^3$ s^{-1} under the SiN gratings, which significantly cancels the surface spin noise of the NV sensor. The relaxation rate Γ_{sig} in the presence of Cyt-C nanoclusters with a concentration of 54 μM is $(2.8 \pm 0.2) \times 10^3$ s^{-1} (Figure 3e). Note that the relaxation rate Γ_s of our specific diamond sensor with very shallow NV centers is the sum of the intrinsic relaxation (Γ_{int}) and the relaxation due to surface spin noise (Γ_{sur}), which accounted for almost half of the relaxation of Γ_s. However, the NV

relaxation rate in the presence of Cyt-C is $\Gamma_{sig} = \Gamma_{int} + \Gamma_{sur} + \Gamma_{ext}$. From the measurements with very low concentrations of Cyt-C proteins (Figure 4d), we found that Γ_{sur} is significantly suppressed by Cyt-C and could be neglected, so that $\Gamma_{ext} \approx \Gamma_{sig} - \Gamma_{int}$.

Cyt-C, being a heme protein with a Fe^{+3} center, can produce fluctuating magnetic fields that interact with NV spins via dipolar-magnetic-interactions.[33,34,49,57] Figures 4a, 4b, and 4c show the Γ_1 images of Cyt-C solution drop-casted onto the diamond substrate with a concentration of 25 μM, 18 μM, and 11 μM, respectively. Figure 4d displays the measured relaxation rate Γ_{ext} (open circles) as a function of the number of Fe^{+3} centers within Cyt-C adsorbed on the diamond surface over 1 μm^2 area. To calibrate our measurements and deduce the NV standoff d from the diamond surface, we measured the relaxation rate Γ_1 in $CuSO_4$ solutions of different concentrations on the diamond substrate and found d of 5.5 nm (see Figure S8 and SI section S8). After that, we calculated the theoretical dependence of Γ_{ext} *versus* the density of Fe^{+3} adsorbed centers per 1 μm^2 (solid line in Figure 4d) by using Equation S1 while keeping the mean dipolar magnetic coupling strength between NV and Fe^{+3} spins in Cyt-C, $\langle B^2 \rangle$, as a free parameter (SI Section S8). For a spin density of 1.7×10^7 Fe^{+3} adsorbed/ μm^2 we determined $\langle B^2 \rangle$ of 0.084 mT.

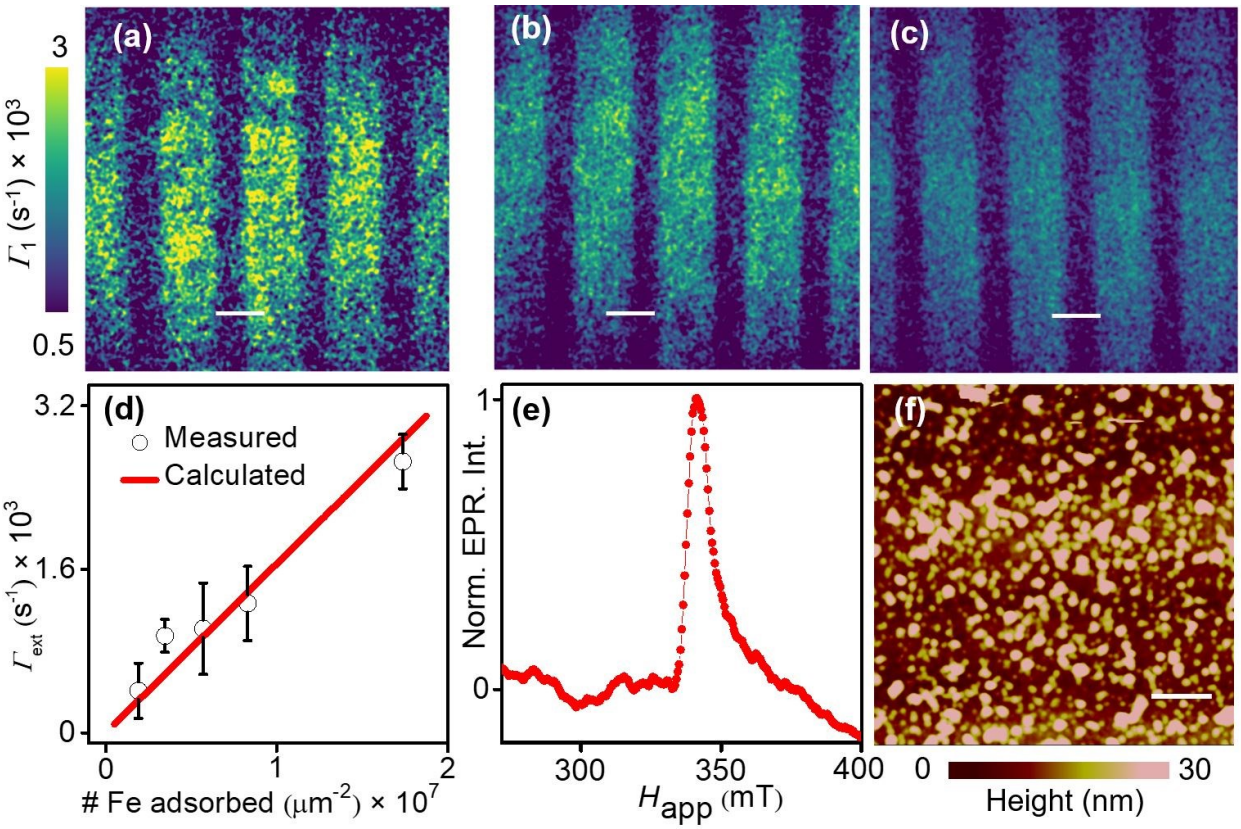

Figure 4. (a) NV Γ_1 map of Cyt-C nanoclusters drop-casted on diamond with a concentration of 25 μM. The bright regions marked the increased relaxation rate due in presence of Cyt-C in contact (no SiN grating) with diamond. The dark regions have SiN due to which the relaxation rate of NV spins gets unaffected. The scale bar is 5 μm. (b) and (c) are the Γ_1 maps in the presence of 18 μM and 11 μM drop-casted Cyt-C nanoclusters, respectively. (d) Measured (open circles) and calculated (solid line) relaxation rate $\Gamma_1 = \Gamma_{ext}$ of NV spins as function of the density of Fe spins adsorbed on the diamond substrate over 1 μm^2 area. (e) Measured EPR spectrum of pelletized 15 mg Cyt-C powder. (f) AFM image (30 μm × 30 μm) taken on

diamond with Cyt-C nanoclusters with a concentration of 54 μM. The AFM image shows the uniform adsorption of Cyt-C proteins on the diamond surface.

EPR spectroscopy was employed to determine the *g*-factor of Fe^{+3} present in Cyt-C proteins and Fe^{+3} transverse spin relaxation T_2^* rate ($\Gamma_2^* = 1/T_2^*$) by analyzing the linewidth of the EPR spectrum (Figure S7). To improve the signal-to-noise ratio of the EPR signal, we generated pellets from the Cyt-C powder by compressing it into a volume of 20 mm^3. We determined an EPR full width at half maximum (FWHM) of 71.43 mT for the pelletized 15 mg Cyt-C powder, corresponding to $\Gamma_2^* \sim 2$ GHz of the Fe^{+3} spins.[34] We also used AFM imaging as an additional method to estimate the Fe^{+3} spin density within Cyt-C, similar to the approach used in reference [49]. Figure 4f shows the AFM image of 30 μm × 30 μm area of Cyt-C nanoclusters at a concentration of 54 μM, drop-casted on the functionalized diamond surface (see Figure 3c for the corresponding Γ_1 image). By measuring the diameter and height of Cyt-C nanoclusters from the AFM image we obtained the volume and therefore the concentration of the drop-casted Cyt-C proteins. For instance, 4 μL of 54 μM Cyt-C was drop-casted on the diamond surface (Figure 4f) for which we obtained a spin density of ~ 1.7×10^7 adsorbed Fe/μm^2. This value agrees well with the calculated Fe^{+3} spin density value based on the NV imaged area of Cyt-C nanoclusters (36 μm × 36 μm).

In conclusion, we demonstrated the variation in concentration of Cyt-C nanocluster (diameter: 50 – 200 nm, height: 5 – 15 nm) using NV T_1 relaxometry through the spin-noise generated by Fe^{+3} spins present in Cyt-C proteins. By patterning the diamond with SiN grating, we performed T_1 relaxometry imaging of Cyt-C nanoclusters with different concentrations. The measured NV relaxation rates agree well with the calculated values deduced from a model of interacting Fe^{+3} paramagnetic centers with NV spins in the diamond substrate with a standoff *d* of 5.5 nm. These results open the door to detect Cyt-C on surface-immobilized microbial cells, with the goal of elucidating the effects of Fe, both in ferrous (Fe^{+2}) and ferric (Fe^{+3}) states, on the electron transport processes during metabolism. The integration of microfluidics[38] and environment control (e.g., no oxygen) to NV magnetometry may allow measuring Cyt-C in different microbes such as *M. sedula*, *R. palustris*, and *M. acetivorans* under aerobic and anaerobic conditions.

Combining NV-T_1 magnetic relaxometry with NV-NMR[29–32] and NV-EPR[58] may enable analyzing Cyt-C inside cells (*in vivo*) or at least in the cell lysates (*in vitro*) by distinguishing the different spin signatures. Quantifying the changes in Cyt-C concentration within the cells is a crucial parameter for assessing cell damage. Consequently, observing the efflux of Cyt-C in living cells proves to be a convenient approach to address apoptosis initiation and monitoring the efficacy of strategies aimed at restoring apoptosis.[59] Using nanodiamonds with longer NV spin relaxation (T_1) and spin coherence (T_2) times[60] functionalized with cells may enable detection of intracellular Cyt-C concentrations.

Associated content

Supporting Information

SEM measurements to confirm the diameter of the Cyt-C nanoclusters, XPS analysis, functionalization of the diamond surface, fabrication of the SiN grating, creation of NV centers in diamond and optical detected magnetic resonance setup, NV magnetic relaxometry imaging, EPR analysis, and theoretical estimation of relaxation rate of NV spins. This material is available free of charge via the Internet at http://pubs.acs.org.

Author Information

Author Contributions

S.L. and R.T. performed NV measurements. C.S. synthesized the cytochrome C powder and functionalized the diamond surface. S.L. performed XPS, AFM, and SEM. I.F and A.L developed the NV-$T1$ relaxometry imaging technique. I.F. helped in analyzing and fitting the measured relaxometry images. K.A. performed EPR measurements. S.-H.L, R.Y.L., and A.L. conceived the cytochrome C study and supervised the project. All authors discussed the results. S.L. and A.L wrote the manuscript with contributions from all authors.

Acknowledgement

This material is based upon work supported by the NSF/EPSCoR RII Track-1: Emergent Quantum Materials and Technologies (EQUATE) Award OIA-2044049, and NSF Award 2328822. I.F. acknowledges support from Latvian Council of Science project lzp- 2021/1-0379. K.A. would like to acknowledge the support of the National Science Foundation/EPSCoR RII Track-4 Award OIA-2033210 and NSF Award 2328822. The research was performed in part in the Nebraska Nanoscale Facility: National Nanotechnology Coordinated Infrastructure and the Nebraska Center for Materials and Nanoscience (and/or NERCF), which are supported by NSF under Award ECCS: 2025298, and the Nebraska Research Initiative. We thank V.M. Acosta for suggesting the fabrication of non-metallic grating on diamond to prevent quenching effects caused by metals.

References

(1) Bertini, I.; Cavallaro, G.; Rosato, A. Cytochrome *c* : Occurrence and Functions. *Chem. Rev.* **2006**, *106* (1), 90–115. https://doi.org/10.1021/cr050241v.

(2) Ow, Y.-L. P.; Green, D. R.; Hao, Z.; Mak, T. W. Cytochrome c: Functions beyond Respiration. *Nat Rev Mol Cell Biol* **2008**, *9* (7), 532–542. https://doi.org/10.1038/nrm2434.

(3) Liu, J.; Chakraborty, S.; Hosseinzadeh, P.; Yu, Y.; Tian, S.; Petrik, I.; Bhagi, A.; Lu, Y. Metalloproteins Containing Cytochrome, Iron–Sulfur, or Copper Redox Centers. *Chem. Rev.* **2014**, *114* (8), 4366–4469. https://doi.org/10.1021/cr400479b.

(4) Kühlbrandt, W. Structure and Function of Mitochondrial Membrane Protein Complexes. *BMC Biol* **2015**, *13* (1), 89. https://doi.org/10.1186/s12915-015-0201-x.

(5) Eleftheriadis, T.; Pissas, G.; Liakopoulos, V.; Stefanidis, I. Cytochrome c as a Potentially Clinical Useful Marker of Mitochondrial and Cellular Damage. *Front. Immunol.* **2016**, *7*. https://doi.org/10.3389/fimmu.2016.00279.

(6) Li, P.; Nijhawan, D.; Budihardjo, I.; Srinivasula, S. M.; Ahmad, M.; Alnemri, E. S.; Wang, X. Cytochrome c and dATP-Dependent Formation of Apaf-1/Caspase-9 Complex Initiates an Apoptotic Protease Cascade. *Cell* **1997**, *91* (4), 479–489. https://doi.org/10.1016/S0092-8674(00)80434-1.

(7) Radhakrishnan, J.; Wang, S.; Ayoub, I. M.; Kolarova, J. D.; Levine, R. F.; Gazmuri, R. J. Circulating Levels of Cytochrome *c* after Resuscitation from Cardiac Arrest: A Marker of Mitochondrial Injury and Predictor of Survival. *American Journal of Physiology-Heart and Circulatory Physiology* **2007**, *292* (2), H767–H775. https://doi.org/10.1152/ajpheart.00468.2006.

(8) Pyka, J.; Osyczka, A.; Turyna, B.; Blicharski, W.; Froncisz, W. EPR Studies of Iso-1-Cytochrome c : Effect of Temperature on Two-Component Spectra of Spin Label Attached to Cysteine at Positions 102 and 47. *European Biophysics Journal* **2001**, *30* (5), 367–373. https://doi.org/10.1007/s002490100168.

(9) Van Son, M.; Schilder, J. T.; Di Savino, A.; Blok, A.; Ubbink, M.; Huber, M. The Transient Complex of Cytochrome c and Cytochrome c Peroxidase: Insights into the Encounter Complex from Multifrequency EPR and NMR Spectroscopy. *ChemPhysChem* **2020**, *21* (10), 1060–1069. https://doi.org/10.1002/cphc.201901160.

(10) Blum, H.; Ohnishi, T. Electron Spin Relaxation of the Electron Paramagnetic Resonance Spectra of Cytochrome c. *Biochimica et Biophysica Acta (BBA) - Protein Structure* **1980**, *621* (1), 9–18. https://doi.org/10.1016/0005-2795(80)90057-4.
(11) Ichimura, K.; Nakahara, Y.; Kimura, K.; Inokuchi, H. Electronic States of Oxidized and Reduced Cytochrome c Observed by X-Ray Photoelectron Spectroscopy. *J. Mater. Chem.* **1992**, *2* (11), 1185. https://doi.org/10.1039/jm9920201185.
(12) Stavis, C.; Clare, T. L.; Butler, J. E.; Radadia, A. D.; Carr, R.; Zeng, H.; King, W. P.; Carlisle, J. A.; Aksimentiev, A.; Bashir, R.; Hamers, R. J. Surface Functionalization of Thin-Film Diamond for Highly Stable and Selective Biological Interfaces. *Proc. Natl. Acad. Sci. U.S.A.* **2011**, *108* (3), 983–988. https://doi.org/10.1073/pnas.1006660107.
(13) Lamichhane, S.; McElveen, K. A.; Erickson, A.; Fescenko, I.; Sun, S.; Timalsina, R.; Guo, Y.; Liou, S.-H.; Lai, R. Y.; Laraoui, A. Nitrogen-Vacancy Magnetometry of Individual Fe-Triazole Spin Crossover Nanorods. *ACS Nano* **2023**, *17* (9), 8694–8704. https://doi.org/10.1021/acsnano.3c01819.
(14) De Gille, R. W.; McCoey, J. M.; Hall, L. T.; Tetienne, J.-P.; Malkemper, E. P.; Keays, D. A.; Hollenberg, L. C. L.; Simpson, D. A. Quantum Magnetic Imaging of Iron Organelles within the Pigeon Cochlea. *Proc. Natl. Acad. Sci. U.S.A.* **2021**, *118* (47), e2112749118. https://doi.org/10.1073/pnas.2112749118.
(15) McCoey, J. M.; Matsuoka, M.; De Gille, R. W.; Hall, L. T.; Shaw, J. A.; Tetienne, J.; Kisailus, D.; Hollenberg, L. C. L.; Simpson, D. A. Quantum Magnetic Imaging of Iron Biomineralization in Teeth of the Chiton *Acanthopleura Hirtosa*. *Small Methods* **2020**, *4* (3), 1900754. https://doi.org/10.1002/smtd.201900754.
(16) Schäfer-Nolte, E.; Schlipf, L.; Ternes, M.; Reinhard, F.; Kern, K.; Wrachtrup, J. Tracking Temperature-Dependent Relaxation Times of Ferritin Nanomagnets with a Wideband Quantum Spectrometer. *Phys. Rev. Lett.* **2014**, *113* (21), 217204. https://doi.org/10.1103/PhysRevLett.113.217204.
(17) Wang, P.; Chen, S.; Guo, M.; Peng, S.; Wang, M.; Chen, M.; Ma, W.; Zhang, R.; Su, J.; Rong, X.; Shi, F.; Xu, T.; Du, J. Nanoscale Magnetic Imaging of Ferritins in a Single Cell. *Sci. Adv.* **2019**, *5* (4), eaau8038. https://doi.org/10.1126/sciadv.aau8038.
(18) Fescenko, I.; Laraoui, A.; Smits, J.; Mosavian, N.; Kehayias, P.; Seto, J.; Bougas, L.; Jarmola, A.; Acosta, V. M. Diamond Magnetic Microscopy of Malarial Hemozoin Nanocrystals. *Phys. Rev. Applied* **2019**, *11* (3), 034029. https://doi.org/10.1103/PhysRevApplied.11.034029.
(19) Doherty, M. W.; Manson, N. B.; Delaney, P.; Jelezko, F.; Wrachtrup, J.; Hollenberg, L. C. L. The Nitrogen-Vacancy Colour Centre in Diamond. *Physics Reports* **2013**, *528* (1), 1–45. https://doi.org/10.1016/j.physrep.2013.02.001.
(20) Laraoui, A.; Dolde, F.; Burk, C.; Reinhard, F.; Wrachtrup, J.; Meriles, C. A. High-Resolution Correlation Spectroscopy of 13C Spins near a Nitrogen-Vacancy Centre in Diamond. *Nat Commun* **2013**, *4* (1), 1651. https://doi.org/10.1038/ncomms2685.
(21) Laraoui, A.; Hodges, J. S.; Meriles, C. A. Magnetometry of Random Ac Magnetic Fields Using a Single Nitrogen-Vacancy Center. *Appl. Phys. Lett.* **2010**, *97* (14), 143104. https://doi.org/10.1063/1.3497004.
(22) Balasubramanian, G.; Neumann, P.; Twitchen, D.; Markham, M.; Kolesov, R.; Mizuochi, N.; Isoya, J.; Achard, J.; Beck, J.; Tissler, J.; Jacques, V.; Hemmer, P. R.; Jelezko, F.; Wrachtrup, J. Ultralong Spin Coherence Time in Isotopically Engineered Diamond. *Nature Mater* **2009**, *8* (5), 383–387. https://doi.org/10.1038/nmat2420.
(23) Degen, C. L.; Reinhard, F.; Cappellaro, P. Quantum Sensing. *Rev. Mod. Phys.* **2017**, *89* (3), 035002. https://doi.org/10.1103/RevModPhys.89.035002.
(24) Casola, F.; van der Sar, T.; Yacoby, A. Probing Condensed Matter Physics with Magnetometry Based on Nitrogen-Vacancy Centres in Diamond. *Nat Rev Mater* **2018**, *3* (1), 1–13. https://doi.org/10.1038/natrevmats.2017.88.
(25) Laraoui, A.; Ambal, K. Opportunities for Nitrogen-Vacancy-Assisted Magnetometry to Study Magnetism in 2D van Der Waals Magnets. *Appl. Phys. Lett.* **2022**, *121* (6), 060502. https://doi.org/10.1063/5.0091931.

(26) Erickson, A.; Shah, S. Q. A.; Mahmood, A.; Fescenko, I.; Timalsina, R.; Binek, C.; Laraoui, A. Nanoscale Imaging of Antiferromagnetic Domains in Epitaxial Films of Cr_2O_3 via Scanning Diamond Magnetic Probe Microscopy. *RSC Adv.* **2022**, *13* (1), 178–185. https://doi.org/10.1039/D2RA06440E.

(27) Aslam, N.; Zhou, H.; Urbach, E. K.; Turner, M. J.; Walsworth, R. L.; Lukin, M. D.; Park, H. Quantum Sensors for Biomedical Applications. *Nat Rev Phys* **2023**, 1–13. https://doi.org/10.1038/s42254-023-00558-3.

(28) Lovchinsky, I.; Sushkov, A. O.; Urbach, E.; de Leon, N. P.; Choi, S.; De Greve, K.; Evans, R.; Gertner, R.; Bersin, E.; Müller, C.; McGuinness, L.; Jelezko, F.; Walsworth, R. L.; Park, H.; Lukin, M. D. Nuclear Magnetic Resonance Detection and Spectroscopy of Single Proteins Using Quantum Logic. *Science* **2016**, *351* (6275), 836–841. https://doi.org/10.1126/science.aad8022.

(29) Degen, C. L.; Poggio, M.; Mamin, H. J.; Rettner, C. T.; Rugar, D. Nanoscale Magnetic Resonance Imaging. *Proc. Natl. Acad. Sci. U.S.A.* **2009**, *106* (5), 1313–1317. https://doi.org/10.1073/pnas.0812068106.

(30) Staudacher, T.; Shi, F.; Pezzagna, S.; Meijer, J.; Du, J.; Meriles, C. A.; Reinhard, F.; Wrachtrup, J. Nuclear Magnetic Resonance Spectroscopy on a (5-Nanometer) ^{3} Sample Volume. *Science* **2013**, *339* (6119), 561–563. https://doi.org/10.1126/science.1231675.

(31) Kehayias, P.; Jarmola, A.; Mosavian, N.; Fescenko, I.; Benito, F. M.; Laraoui, A.; Smits, J.; Bougas, L.; Budker, D.; Neumann, A.; Brueck, S. R. J.; Acosta, V. M. Solution Nuclear Magnetic Resonance Spectroscopy on a Nanostructured Diamond Chip. *Nat Commun* **2017**, *8* (1), 188. https://doi.org/10.1038/s41467-017-00266-4.

(32) Smits, J.; Damron, J. T.; Kehayias, P.; McDowell, A. F.; Mosavian, N.; Fescenko, I.; Ristoff, N.; Laraoui, A.; Jarmola, A.; Acosta, V. M. Two-Dimensional Nuclear Magnetic Resonance Spectroscopy with a Microfluidic Diamond Quantum Sensor. *Sci. Adv.* **2019**, *5* (7), eaaw7895. https://doi.org/10.1126/sciadv.aaw7895.

(33) Steinert, S.; Ziem, F.; Hall, L. T.; Zappe, A.; Schweikert, M.; Götz, N.; Aird, A.; Balasubramanian, G.; Hollenberg, L.; Wrachtrup, J. Magnetic Spin Imaging under Ambient Conditions with Sub-Cellular Resolution. *Nat Commun* **2013**, *4* (1), 1607. https://doi.org/10.1038/ncomms2588.

(34) Simpson, D. A.; Ryan, R. G.; Hall, L. T.; Panchenko, E.; Drew, S. C.; Petrou, S.; Donnelly, P. S.; Mulvaney, P.; Hollenberg, L. C. L. Electron Paramagnetic Resonance Microscopy Using Spins in Diamond under Ambient Conditions. *Nat Commun* **2017**, *8* (1), 458. https://doi.org/10.1038/s41467-017-00466-y.

(35) Nie, L.; Nusantara, A. C.; Damle, V. G.; Sharmin, R.; Evans, E. P. P.; Hemelaar, S. R.; Van Der Laan, K. J.; Li, R.; Perona Martinez, F. P.; Vedelaar, T.; Chipaux, M.; Schirhagl, R. Quantum Monitoring of Cellular Metabolic Activities in Single Mitochondria. *Sci. Adv.* **2021**, *7* (21), eabf0573. https://doi.org/10.1126/sciadv.abf0573.

(36) Wojtas, D.; Li, R.; Jarzębska, A.; Sułkowski, B.; Zehetbauer, M.; Schafler, E.; Wierzbanowski, K.; Mzyk, A.; Schirhagl, R. Quantum Sensing for Detection of Zinc-Triggered Free Radicals in Endothelial Cells. *Adv Quantum Tech* **2023**, *6* (11), 2300174. https://doi.org/10.1002/qute.202300174.

(37) Nie, L.; Nusantara, A. C.; Damle, V. G.; Baranov, M. V.; Chipaux, M.; Reyes-San-Martin, C.; Hamoh, T.; Epperla, C. P.; Guricova, M.; Cigler, P.; Van Den Bogaart, G.; Schirhagl, R. Quantum Sensing of Free Radicals in Primary Human Dendritic Cells. *Nano Lett.* **2022**, *22* (4), 1818–1825. https://doi.org/10.1021/acs.nanolett.1c03021.

(38) Wu, K.; Vedelaar, T. A.; Damle, V. G.; Morita, A.; Mougnaud, J.; Reyes San Martin, C.; Zhang, Y.; Van Der Pol, D. P. I.; Ende-Metselaar, H.; Rodenhuis-Zybert, I.; Schirhagl, R. Applying NV Center-Based Quantum Sensing to Study Intracellular Free Radical Response upon Viral Infections. *Redox Biology* **2022**, *52*, 102279. https://doi.org/10.1016/j.redox.2022.102279.

(39) Mugnol, K. C. U.; Ando, R. A.; Nagayasu, R. Y.; Faljoni-Alario, A.; Brochsztain, S.; Santos, P. S.; Nascimento, O. R.; Nantes, I. L. Spectroscopic, Structural, and Functional Characterization of the Alternative Low-Spin State of Horse Heart Cytochrome c. *Biophysical Journal* **2008**, *94* (10), 4066–4077. https://doi.org/10.1529/biophysj.107.116483.

(40) Miyashita, Y.; Wazawa, T.; Mogami, G.; Takahashi, S.; Sambongi, Y.; Suzuki, M. Hydration-State Change of Horse Heart Cytochrome c Corresponding to Trifluoroacetic-Acid-Induced Unfolding. *Biophysical Journal* **2013**, *104* (1), 163–172. https://doi.org/10.1016/j.bpj.2012.11.3825.
(41) Gong, Y.; Liu, Q.; Wilt, J. S.; Gong, M.; Ren, S.; Wu, J. Wrapping Cytochrome c around Single-Wall Carbon Nanotube: Engineered Nanohybrid Building Blocks for Infrared Detection at High Quantum Efficiency. *Sci Rep* **2015**, *5* (1), 11328. https://doi.org/10.1038/srep11328.
(42) Nucara, A.; Carbone, M.; Ripanti, F.; Manganiello, R.; Postorino, P.; Carbonaro, M. Achieving Cytochrome c Fibril/Aggregate Control towards Micro-Platelets and Micro-Fibers by Tuning pH and Protein Concentration: A Combined Morphological and Spectroscopic Analysis. *International Journal of Biological Macromolecules* **2019**, *138*, 106–115. https://doi.org/10.1016/j.ijbiomac.2019.07.060.
(43) Mirkin, N.; Jaconcic, J.; Stojanoff, V.; Moreno, A. High Resolution X-Ray Crystallographic Structure of Bovine Heart Cytochrome c and Its Application to the Design of an Electron Transfer Biosensor. *Proteins* **2007**, *70* (1), 83–92. https://doi.org/10.1002/prot.21452.
(44) Hirota, S.; Hattori, Y.; Nagao, S.; Taketa, M.; Komori, H.; Kamikubo, H.; Wang, Z.; Takahashi, I.; Negi, S.; Sugiura, Y.; Kataoka, M.; Higuchi, Y. Cytochrome *c* Polymerization by Successive Domain Swapping at the C-Terminal Helix. *Proc. Natl. Acad. Sci. U.S.A.* **2010**, *107* (29), 12854–12859. https://doi.org/10.1073/pnas.1001839107.
(45) Descostes, M.; Mercier, F.; Thromat, N.; Beaucaire, C.; Gautier-Soyer, M. Use of XPS in the Determination of Chemical Environment and Oxidation State of Iron and Sulfur Samples: Constitution of a Data Basis in Binding Energies for Fe and S Reference Compounds and Applications to the Evidence of Surface Species of an Oxidized Pyrite in a Carbonate Medium. *Applied Surface Science* **2000**, *165* (4), 288–302. https://doi.org/10.1016/S0169-4332(00)00443-8.
(46) Isaacson, Y. A.; Majuk, Z.; Brisk, M. A.; Gellender, M. E.; Baker, A. D. Iron to Sulfur Bonding in Cytochrome c Studied by X-Ray Photoelectron Spectroscopy. *J. Am. Chem. Soc.* **1975**, *97* (22), 6603–6604. https://doi.org/10.1021/ja00855a067.
(47) Jarmola, A.; Acosta, V. M.; Jensen, K.; Chemerisov, S.; Budker, D. Temperature- and Magnetic-Field-Dependent Longitudinal Spin Relaxation in Nitrogen-Vacancy Ensembles in Diamond. *Phys. Rev. Lett.* **2012**, *108* (19), 197601. https://doi.org/10.1103/PhysRevLett.108.197601.
(48) Mzyk, A.; Sigaeva, A.; Schirhagl, R. Relaxometry with Nitrogen Vacancy (NV) Centers in Diamond. *Acc. Chem. Res.* **2022**, *55* (24), 3572–3580. https://doi.org/10.1021/acs.accounts.2c00520.
(49) Ziem, F. C.; Götz, N. S.; Zappe, A.; Steinert, S.; Wrachtrup, J. Highly Sensitive Detection of Physiological Spins in a Microfluidic Device. *Nano Lett.* **2013**, *13* (9), 4093–4098. https://doi.org/10.1021/nl401522a.
(50) Kleinsasser, E. E.; Stanfield, M. M.; Banks, J. K. Q.; Zhu, Z.; Li, W.-D.; Acosta, V. M.; Watanabe, H.; Itoh, K. M.; Fu, K.-M. C. High Density Nitrogen-Vacancy Sensing Surface Created via He+ Ion Implantation of 12C Diamond. *Appl. Phys. Lett.* **2016**, *108* (20), 202401. https://doi.org/10.1063/1.4949357.
(51) Huang, L.-C. L.; Chang, H.-C. Adsorption and Immobilization of Cytochrome *c* on Nanodiamonds. *Langmuir* **2004**, *20* (14), 5879–5884. https://doi.org/10.1021/la0495736.
(52) Mrózek, M.; Rudnicki, D.; Kehayias, P.; Jarmola, A.; Budker, D.; Gawlik, W. Longitudinal Spin Relaxation in Nitrogen-Vacancy Ensembles in Diamond. *EPJ Quantum Technol.* **2015**, *2* (1), 1–11. https://doi.org/10.1140/epjqt/s40507-015-0035-z.
(53) Laraoui, A.; Hodges, J. S.; Meriles, C. A. Nitrogen-Vacancy-Assisted Magnetometry of Paramagnetic Centers in an Individual Diamond Nanocrystal. *Nano Lett.* **2012**, *12* (7), 3477–3482. https://doi.org/10.1021/nl300964g.
(54) Laraoui, A.; Meriles, C. A. Approach to Dark Spin Cooling in a Diamond Nanocrystal. *ACS Nano* **2013**, *7* (4), 3403–3410. https://doi.org/10.1021/nn400239n.
(55) Sangtawesin, S.; Dwyer, B. L.; Srinivasan, S.; Allred, J. J.; Rodgers, L. V. H.; De Greve, K.; Stacey, A.; Dontschuk, N.; O'Donnell, K. M.; Hu, D.; Evans, D. A.; Jaye, C.; Fischer, D. A.; Markham, M. L.; Twitchen, D. J.; Park, H.; Lukin, M. D.; de Leon, N. P. Origins of Diamond Surface Noise Probed by

Correlating Single-Spin Measurements with Surface Spectroscopy. *Phys. Rev. X* **2019**, *9* (3), 031052. https://doi.org/10.1103/PhysRevX.9.031052.

(56) Ariyaratne, A.; Bluvstein, D.; Myers, B. A.; Jayich, A. C. B. Nanoscale Electrical Conductivity Imaging Using a Nitrogen-Vacancy Center in Diamond. *Nat Commun* **2018**, *9* (1), 2406. https://doi.org/10.1038/s41467-018-04798-1.

(57) Hall, L. T.; Kehayias, P.; Simpson, D. A.; Jarmola, A.; Stacey, A.; Budker, D.; Hollenberg, L. C. L. Detection of Nanoscale Electron Spin Resonance Spectra Demonstrated Using Nitrogen-Vacancy Centre Probes in Diamond. *Nat Commun* **2016**, *7* (1), 10211. https://doi.org/10.1038/ncomms10211.

(58) Shi, F.; Zhang, Q.; Wang, P.; Sun, H.; Wang, J.; Rong, X.; Chen, M.; Ju, C.; Reinhard, F.; Chen, H.; Wrachtrup, J.; Wang, J.; Du, J. Single-Protein Spin Resonance Spectroscopy under Ambient Conditions. *Science* **2015**, *347* (6226), 1135–1138. https://doi.org/10.1126/science.aaa2253.

(59) Pessoa, J. Live-Cell Visualization of Cytochrome *c* : A Tool to Explore Apoptosis. *Biochemical Society Transactions* **2021**, *49* (6), 2903–2915. https://doi.org/10.1042/BST20211028.

(60) Trusheim, M. E.; Li, L.; Laraoui, A.; Chen, E. H.; Bakhru, H.; Schröder, T.; Gaathon, O.; Meriles, C. A.; Englund, D. Scalable Fabrication of High Purity Diamond Nanocrystals with Long-Spin-Coherence Nitrogen Vacancy Centers. *Nano Lett.* **2014**, *14* (1), 32–36. https://doi.org/10.1021/nl402799u.

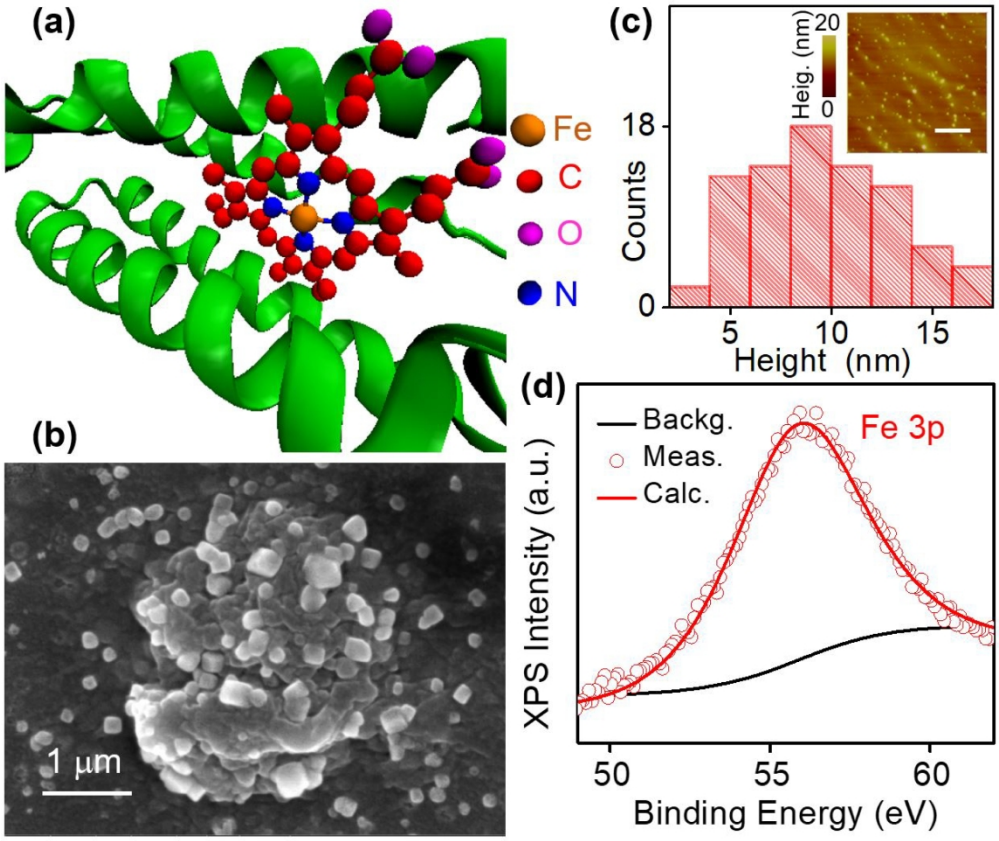

(a) Molecular structure of Cyt-C complex derived from reference [1]. (b) SEM image of 18 μM Cyt-C drop-casted on a carbon tape to prevent charging effect. (c) AFM height distribution of Cyt-C nanoclusters (concentration of 2 μM) drop-cased on top of the diamond substrate. The mean height of Cyt-C nanoclusters is ~ 9 ± 6 nm. Inset of (c): AFM image of the Cyt-C nanoclusters (the scale bar is 5 μm). (d) Measured (open circles) XPS spectra of Fe 3p in Cyt-C with the fitting (red solid line) showing the Fe^{+3} state. The background signal is plotted in the black solid line curve.

329x277mm (300 x 300 DPI)

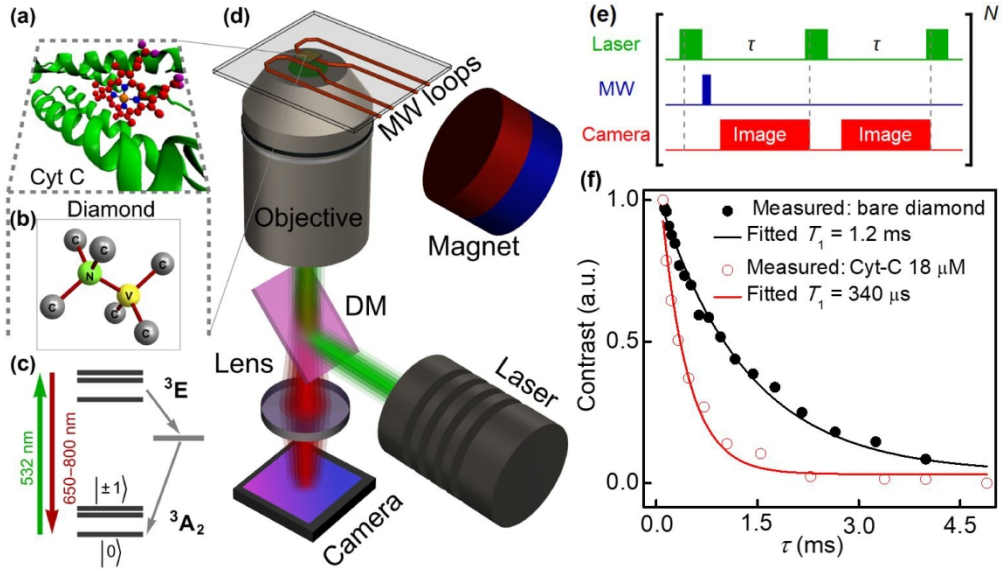

(a) Molecular structure of Cyt-C protein. (b) A schematic of the NV center inside the diamond lattice (nitrogen: green atom, yellow: vacancy). (c) A schematic of the energy levels of the NV center ground ($^3A^2$) and excited (^{3}E) states with intermediate metastable state. A green laser (532 nm) initializes the NV center spins and results in fluorescence in wavelength range of 650 – 800 nm. (d) A schematic of the widefield NV microscope used for T_1 relaxometry measurements and imaging of Cyt-C nanoclusters. DM is the dichroic mirror. (e) A schematic of a pulse sequence for T_1 relaxometry imaging. (f) T_1 curve measured on a bare diamond (filled circles) and after drop-casting 18 μM Cyt-C solution on diamond (open circles). The black and red solid lines are exponential decay function fits of the measured T_1 relaxation curves.

406x230mm (300 x 300 DPI)

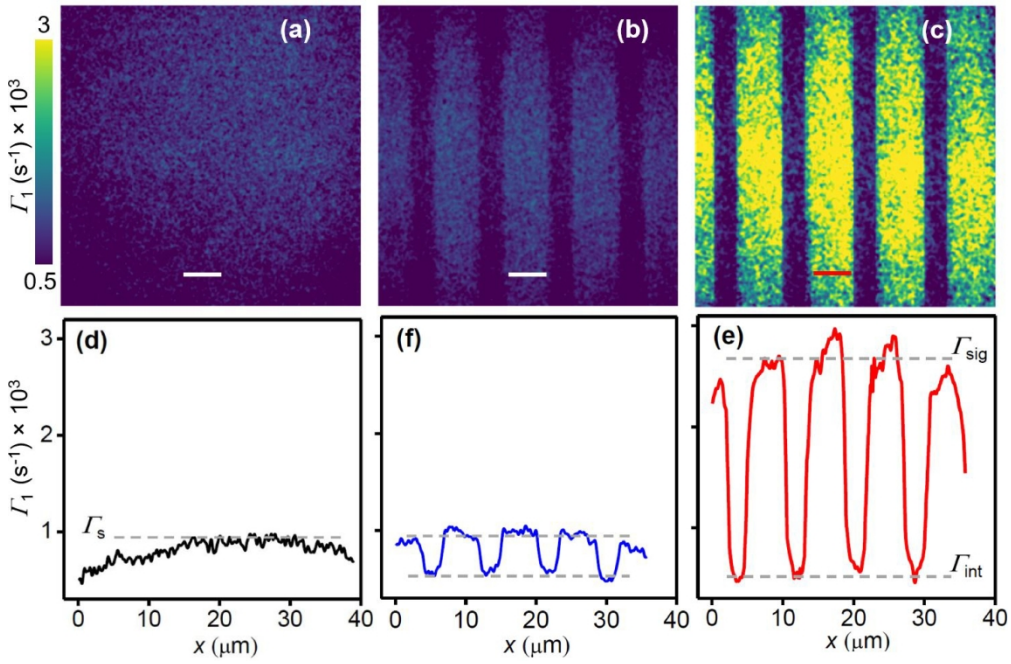

Γ_1 maps acquired by pixelwise exponential fitting of series of maps of the ODMR contrast decays for (a) clean bare diamond, (b) clean diamond with the SiN grating, and (c) Cyt-C with a concentration of 54 μM drop-casted on the diamond with SiN grating. The scale bar in (a), (b), and (c) is 5 μm. Corresponding extracted horizontal Γ_1 profiles from the measurements done on bare diamond (d), diamond with SiN grating and no Cyt-C (f), and diamond with SiN and Cyt-C (e).

390x257mm (300 x 300 DPI)

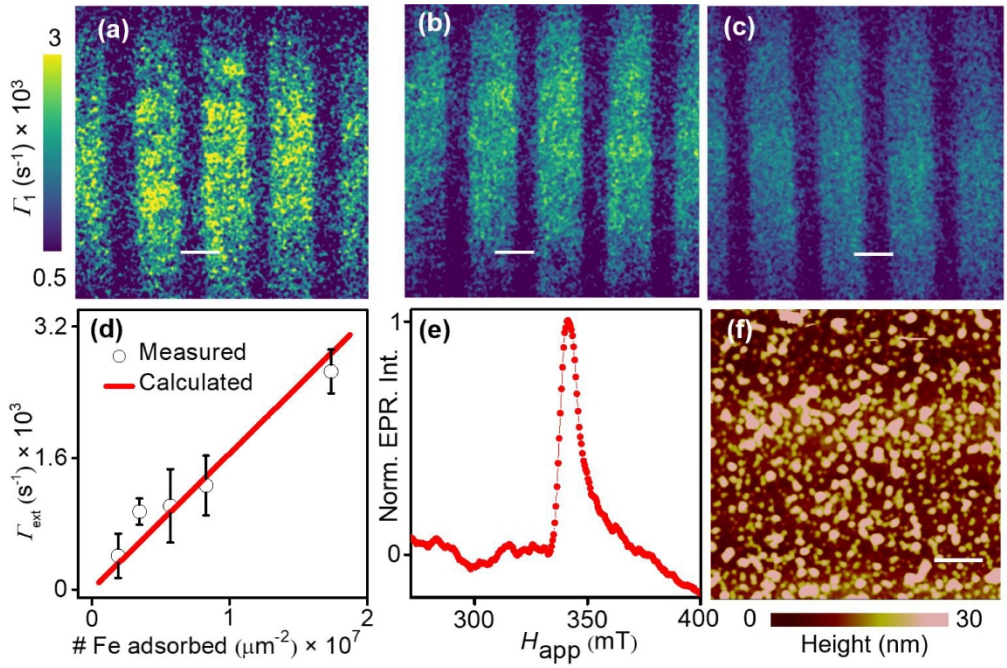

(a) NV Γ_1 map of Cyt-C nanoclusters drop-casted on diamond with a concentration of 25 μM. The bright regions marked the increased relaxation rate due in presence of Cyt-C in contact (no SiN grating) with diamond. The dark regions have SiN due to which the relaxation rate of NV spins gets unaffected. The scale bar is 5 μm. (b) and (c) are the Γ_1 maps in the presence of 18 μM and 11 μM drop-casted Cyt-C nanoclusters, respectively. (d) Measured (open circles) and calculated (solid line) relaxation rate $\Gamma_1 = \Gamma_{ext}$ of NV spins as function of the density of Fe spins adsorbed on the diamond substrate over 1 μm^2 area. (e) Measured EPR spectrum of pelletized 15 mg Cyt-C powder. (f) AFM image (30 μm × 30 μm) taken on diamond with Cyt-C nanoclusters with a concentration of 54 μM. The AFM image shows the uniform adsorption of Cyt-C proteins on the diamond surface.

401x266mm (300 x 300 DPI)

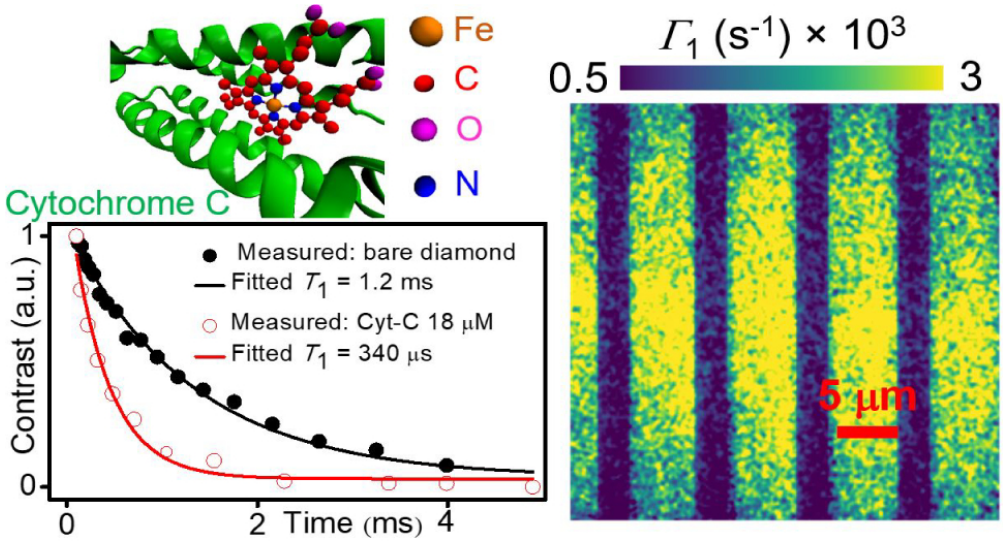

81x44mm (300 x 300 DPI)